Bone 121 (2019) 89–99

Contents lists available at ScienceDirect

Bone

journal homepage: www.elsevier.com/locate/bone

Full Length Article

3D patient-specific finite element models of the proximal femur based on DXA towards the classification of fracture and non-fracture cases

Carlos Ruiz Wills[a,*], Andy Luis Olivares[a], Simone Tassani[a], Mario Ceresa[a], Veronika Zimmer[a,b], Miguel A. González Ballester[a,c], Luis Miguel del Río[d], Ludovic Humbert[e], Jérôme Noailly[a]

[a] BCN MedTech, Universitat Pompeu Fabra (UPF), Barcelona, Spain
[b] School of Biomedical Engineering & Imaging Sciences, King's College London, London, UK
[c] ICREA, Barcelona, Spain
[d] CETIR Medical Group, Barcelona, Spain
[e] Galgo Medical SL, Barcelona, Spain

ARTICLE INFO

Keywords:
Hip fracture
DXA
3D finite element analysis
Fracture discrimination

ABSTRACT

Osteoporotic bone fractures reduce quality of life and drastically increase mortality. Minimally irradiating imaging techniques such as dual-energy X-ray absorptiometry (DXA) allow assessment of bone loss through the use of bone mineral density (BMD) as descriptor. Yet, the accuracy of fracture risk predictions remains limited. Recently, DXA-based 3D modelling algorithms were proposed to analyse the geometry and BMD spatial distribution of the proximal femur. This study hypothesizes that such approaches can benefit from finite element (FE)-based biomechanical analyses to improve fracture risk prediction. One hundred and eleven subjects were included in this study and stratified in two groups: (a) 62 fracture cases, and (b) 49 non-fracture controls. Side fall was simulated using a static peak load that depended on patient mass and height. Local mechanical fields were calculated based on relationships between tissue stiffness and BMD. The area under the curve (AUC) of the receiver operating characteristic method evaluated the ability of calculated biomechanical descriptors to discriminate fracture and control cases. The results showed that the major principal stress was better discriminator (AUC $>$ 0.80) than the volumetric BMD (AUC $\leq$ 0.70). High discrimination capacity was achieved when the analysis was performed by bone type, zone of fracture and gender/sex (AUC of 0.91 for women, trabecular bone and trochanter area), and outcomes suggested that the trabecular bone is critical for fracture discrimination. In conclusion, 3D FE models derived from DXA scans might significantly improve the prediction of hip fracture risk; providing a new insight for clinicians to use FE simulations in clinical practice for osteoporosis management.

1. Introduction

Osteoporosis reduces the bone density altering bone strength [1,2]. This reduction of bone strength increases the risk of fracture [3,4]. Among all osteoporotic fractures, hip fractures are a major problem in western countries [5–7]. In fact, this fracture is estimated to affect one third and one fifth of women and men, respectively [8]. The trauma reduces mobility, quality of life and even can increase the mortality in both women and men [3,9,10]. As such, the prediction of osteoporotic hip fractures is highly important for clinicians [11,12].

Bone mineral density (BMD) is used to identify patients with osteoporosis. The gold standard to measure BMD is dual energy X-ray absorptiometry (DXA) thanks to its low cost and to low exposure of patients to radiation [13]. Areal BMD (aBMD) obtained by DXA was used for the discrimination of fracture and control cases with values of area under the curve (AUC) around 0.70 [9,14,15]. Yet, 2D measurements such as aBMD do not provide information about BMD spatial distribution. In contrast to DXA, quantitative computed tomography (QCT) provides distribution of the volumetric BMD (vBMD) and separate the measurements for cortical and trabecular bone. vBMD can be used to determine bone material properties like stiffness and strength, standing for a great asset for bone fracture prediction [16]. However, QCT exposes the patient to a higher radiation compared to DXA, the availability of devices is limited and the cost is relatively high, which limits the use of QCT for routine patient explorations and monitoring [17].

Some diagnostic tools are available to calculate the risk of fracture, being the fracture risk assessment (FRAX) the most popular one, where patient data are compared to a large database that includes many

* Corresponding author at: C/ Roc Boronat, 138, 08018 Barcelona, Spain.
E-mail address: carlos.ruiz@upf.edu (C. Ruiz Wills).

https://doi.org/10.1016/j.bone.2019.01.001
Received 30 July 2018; Received in revised form 21 December 2018; Accepted 1 January 2019
Available online 03 January 2019
8756-3282/

features, e.g. age, gender, country. Nevertheless, FRAX fracture prediction error is around 25–30% [18]. Bone metabolic markers, including formation, resorption, and matrix markers, are also employed for the evaluation of the bone quality and the risk of fracture [19]. Although these biomarkers might be used for treatment monitoring of osteoporosis, their clinical value for fracture risk assessment is limited due to insufficient control of quality, scarce data for treatment comparisons with the same marker, and deficient capacity to evaluate source variations [1].

Quantification of the mechanical behaviour of the bone for fracture prediction was generally addressed using finite element (FE) models [20]. Poor accuracy in geometry, bone material properties and validation were the main challenges for early FE models. The combination of QTC imagining and FE models provided, however, a new generation of patient-specific models that allowed exploring the effects of different mechanical scenarios. Schileo et al. [21] developed an experimental-numerical study to evaluate how QCT acquisition parameters, ash BMD (ash weight divided by the real volume) and apparent BMD (density measured in fresh and wet conditions) affect the precision of patient-specific FE models. They showed that the calibration of the relationship between QCT BMD and ash BMD, and the definition of the ratio of ash BMD to apparent BMD highly altered the strain fields predicted by the models. Nevertheless, Nishiyama et al. [22] used a QCT-based FE model classify 35 women with and without hip fracture through bone strength, and found that combining vBMD and FE model calculations led to a classification accuracy over 90%. Recently, Qasim et al. [15] studied how the image protocol used to generate patient-specific FE models can affect the discrimination power of the femoral strength. Yet, their results also revealed that the FE-strength obtained by QCT-based models simulations is a reliable predictor and it is better than aBMD for fracture discrimination.

Recently, 3D models could be generated from DXA images [23,24]. Humbert et al. [23] used DXA projections to extrapolate the density distribution in 3D for trabecular and cortical regions, the femoral shape of the femur, and also the cortical thickness. They found correlation coefficients of 0.86, 0.93 and 0.91 between 3D-DXA and QCT measurements for the extrapolated vBMD in the trabecular and cortical regions, and for the mean cortical thickness, respectively. Grassi et al. [25] used a 3D FE model obtained from 2D DXA images to estimate the bone strength. Their results showed that the estimated principal strains and femoral strength were comparable with the results obtained by 3D QCT-based models but the potential of the calculated parameters for clinical classification in terms of fracture risk was not tested.

Hence, the aim of this study is to find biomechanical criteria for the discrimination of proximal femur fracture towards fracture risk classification, by exploiting DXA-derived 3D models and patient-specific FE simulations in an in vivo context.

2. Materials and methods

2.1. Subject recruitment

DXA femur scans were performed at CETIR Medical Group for patients of both sexes, older than 50 years, with clinical risk factors of osteoporosis that supported the prescription of BMD measurement. Subjects with hip fracture were recruit after entering the emergency room of the Hospital Mutua de Terrassa, where neck or tranchanter fracture was confirmed by symptoms, clinical explorations and X-rays. An evaluation for surgical treatment was performed for 98% of the fracture cases, and a densitometry exploration of the subject was indicated either at the end of the stay at the hospital or after discharge. The time between the occurrence of the fracture and the DXA exploration never exceeded two weeks. DXA acquisitions were taken on the femur opposite to the fracture. In all cases, the first pelvis-femoral X-rays were evaluated to identify the fracture lines and bone fragments. The patients signed an informed consent document for the scientific use of the radiological explorations and associated clinical data. Documents and methodology were approved by the ethical committee of the Hospital Mutua de Terrasa (Terrasa, Spain). The guidelines of good clinical practice of the Declaration of Helsinki were followed, and the DXA scans were performed considering the standards of the manufacturer of the densitometer (see Section 2.2).

2.2. Image acquisition

A GE Healthcare DXA bone densitometer (GE Healthcare, Madison, WI, USA), model Prodigy Advance, was used to perform the scans. The device uses a narrow angle fan-bean that produces double X-Ray energies using an X-Ray constant cerium K-filter. The detector head has an energy sensitive solid-state array direct-digital CZT (Cadmiun Zinc Telluride) that produces a 2D-image of the bone mineral content X-Ray attenuation without magnification.

All patients were positioned and scanned considering the manufacturer recommendations. The subjects were placed on the DXA table in prone position, with the feet together, and internal rotation of the leg to be scanned of 25–30°. The enCore™ software platform (GE Healthcare) was used to perform the hip DXA scans.

2.3. Subject-specific model generation

2.3.1. Shape and density 3D modelling

Subject-specific 3D models were obtained from the DXA images using the 3D-Shaper® software (version 2.6, Galgo Medical, Barcelona, Spain). Details of the modelling method implemented in the software can be found in [23]. Briefly, the algorithm uses a 3D statistical shape and density model of the proximal femur built from a database of QCT scans of Caucasian men and women. The database included 111 subjects (30 male and 81 female) with a mean age of 56.2 ± 12.1 years (30 years–84 years). Exclusion criteria for all subjects included skeletal disease other than osteoporosis, such as osteoarthritis or Paget's disease, as well as previous hip fracture. The statistical model is registered onto the DXA scan to obtain a subject-specific 3D model of the proximal femur (femoral shape and 3D bone density image). The cortex is segmented in the 3D bone density image by fitting a function of the cortical thickness and density, the location of the cortex, the density of surrounding tissues, and the imaging blur to the density profile computed along the normal vector at each node of the proximal femur surface mesh [26]. The software provides vBMD measurements of the trabecular and cortical bone, a surface mesh of the femoral shape with information of cortical thickness and density at each vertex, and a 3D image of the vBMD distribution. Accuracy of 3D-SHAPER models and measurements was evaluated against QCT in previous work [23]. In brief, 157 subjects (57 male and 100 female) with a mean age of 57.5 ± 13.5 years (23 years–91 years) were included in this validation study. The mean shape accuracy, i.e. the mean distance between the external boundaries of the 3D-SHAPER- and QCT-derived femur geometries, was 0.93 mm. As for the bone density and cortical bone thickness, the correlation coefficients between 3D-SHAPER and QCT-derived measurements were 0.86, 0.93 and 0.91 for the trabecular vBMD, cortical vBMD and cortical thickness, respectively. Similar accuracy was obtained when the method was evaluated using DXA scanners from different manufacturers.

2.3.2. Generic FE mesh

A generic 3D geometry of the femur was created over the mean shape of the statistical model used in the 3D modelling process. The 3D surface shape was divided into 5 sections, which were further divided to obtain face-like surfaces (Fig. 1). For the creation of each 3D solids, six face-like surface were needed. Some sections needed additional faces to complete the face-like surfaces needed to create the 3D paralepidid-like solid of the section. 3D solids were created from the projections of the faces using the open-source software Salome (http://www.salome-platform.org/) (Fig. 1). The full 3D geometry of the femur was

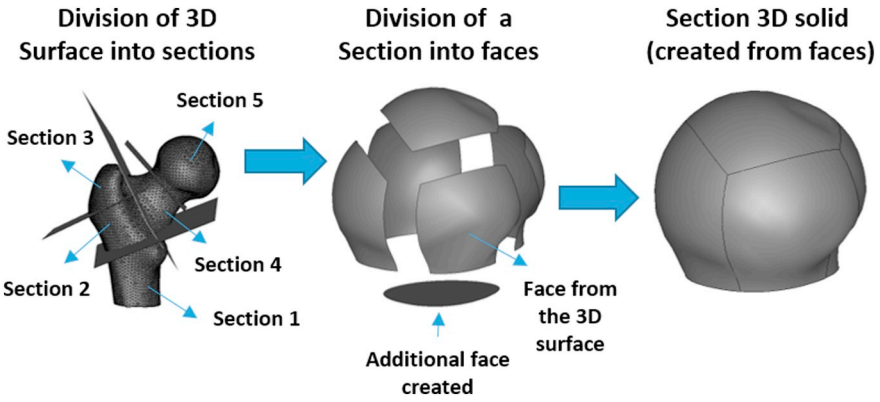

Fig. 1. Scheme for the generation of each 3D solid needed to build the femur geometry.

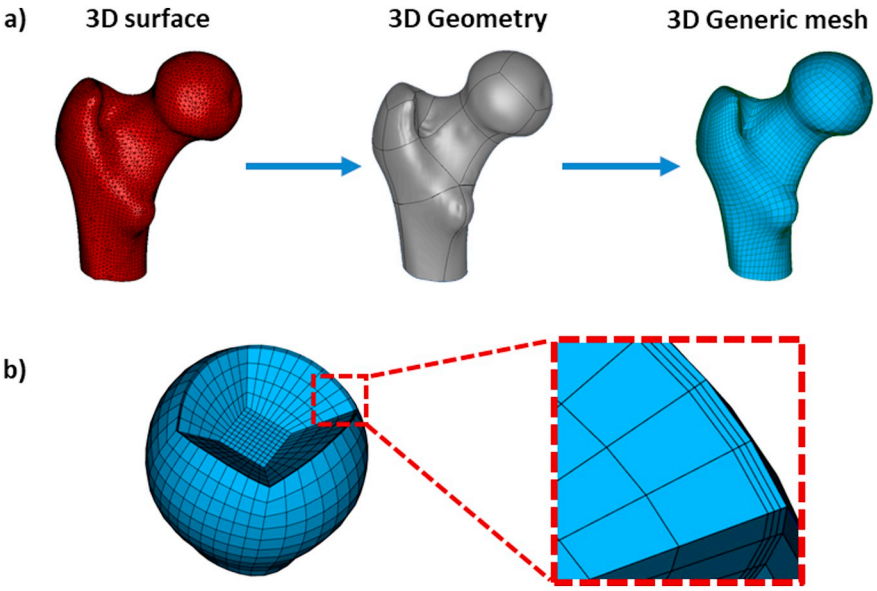

Fig. 2. a) Generation of the generic volume mesh from the mean the surface shape of the statistical model used in the 3D-Shaper® modelling process, b) Femoral head internal mesh. The zoom area shows the layer of three elements modelling the cortical bone.

obtained by merging all solids created (Fig. 2a). Then, a structured FE mesh of hexahedrons was developed for this geometry using Salome (Fig. 2a). A fine layer of three elements was created from the surface of the femur to the interior for the cortical bone (Fig. 2b). The suitability of the mesh density was evaluated through a mesh convergence study. To test mesh convergence, three models were used: model 1 with 26,200 elements, model 2 with 126,800 elements and model 3 with 334,800 elements. The bottom of the proximal femur model was fixed and an axial load of 6000 N was applied on the femoral head. The strain energy density (SED) was evaluated in the neck area of the femur to check the numerical convergence errors associated with the size of the mesh. Simulations were made with a desktop computer Intel® Xeon®, 2CPU, 2.67 GHz, with 12.0 GB RAM.

2.3.3. Subject-specific 3D mesh

This step tackles the transformation of the generic hexahedral mesh created in Section 2.3.2 (initial model) into a patient-specific FE geometrical model (target model). Dense deformation fields that describe the morphing of the generic FE model towards the subject-specific femur were calculated. To this end, we used thin-plate splines (TPS) to interpolate the movement of points over scattered data [27,28]. TPS describes the morphing process as the bending of a thin plate of metal in which the deformation of the plane represents the required transformation of the coordinates.

To perform the matching, we define a set of N points $p_i = [p_1\ p_2\ p_3]^T$ on the initial model to be matched with the corresponding points $q_i = [q_1\ q_2\ q_3]^T$ in the target model. A coordinate transformation $f(x_i) = p(x_i) - q(x_i)$ must be determined such as x equals the displacements at the control points and interpolate them elsewhere.

As the plate has some rigidity that resists the deformation, the transformation that we seek requires the minimization of an energy, called the "bending" energy, that describes the mapping between the original and target points and penalizes non-smooth solutions:

$$E(f) = \sum_{i=1}^{K} \|p_i - f(x_i)\|^2 - \lambda\phi[f] \tag{1}$$

where $f(x_i)$ is the displacement function that we want to calculate, the first term is the approximation error between the target and original points and the $\phi[\cdot]$ is a stabilizer operator that enforces the smoothness of the solution; λ is a parameter that controls the importance of the stabilizer. A possible choice for $\phi[\cdot]$ is:

$$\phi[f] = \iiint \left[\left(\frac{\partial^2 f}{\partial x_1^2}\right)^2 + \left(\frac{\partial^2 f}{\partial x_2^2}\right)^2 + \left(\frac{\partial^2 f}{\partial x_3^2}\right)^2 + 2\left(\frac{\partial^2 f}{\partial x_1 \partial x_2}\right)^2 + 2\left(\frac{\partial^2 f}{\partial x_1 \partial x_3}\right)^2 + 2\left(\frac{\partial^2 f}{\partial x_2 \partial x_3}\right)^2 \right] dx_1 dx_2 dx_3 \tag{2}$$

The solution can be interpolated using a weighted combination of thin plate equations centered on the control points:

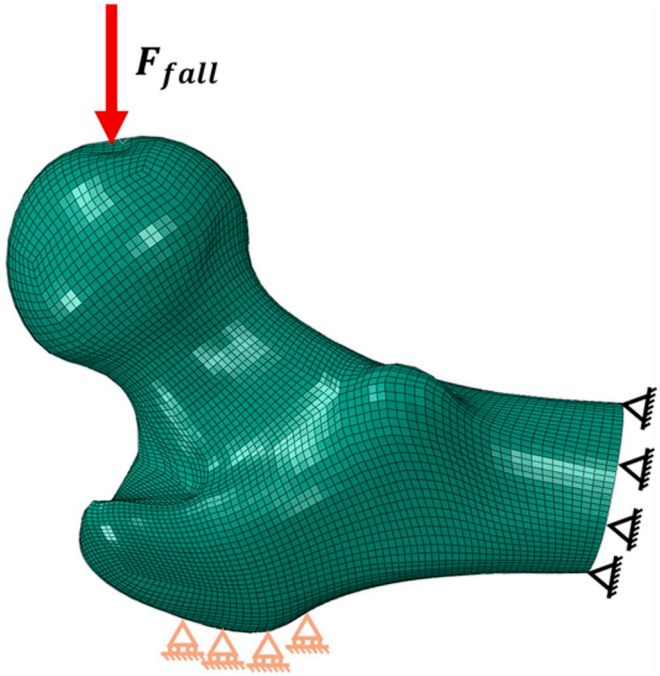

Fig. 3. Boundary conditions used for the simulation of the lateral fall.

$$f(x_i) = a_1 + a_2 x_{i1} + a_3 x_{i2} + a_4 x_{i3} + \sum_{j=1}^{n} \omega_j U(|x_i - p_j|) \quad (3)$$

$$U(r_{ij}) = r_{ij}^2 ln(r_{ij}^2) \text{ with } r_{ij} = \sqrt{(x_{i1} - p_{j1})^2 + (x_{i2} - p_{j2})^2 + (x_{i3} - p_{j3})^2} \quad (4)$$

The definition of n control points, P_i (x_{i1}, x_{i2}, x_{i3}) (n was varied to optimize the approximation of the morphed surface) in the final model led to the ($3 \times n$) matrix of points P, and to the ($n \times n$) kernel matrix K:

$$P = \begin{pmatrix} x_{11} & x_{21} & x_{31} \\ x_{12} & x_{22} & x_{32} \\ \vdots & \vdots & \vdots \\ x_{1n} & x_{2n} & x_{3n} \end{pmatrix} \quad (5)$$

$$K = \begin{pmatrix} 0 & U(r_{12}) & \dots & U(r_{1n}) \\ U(r_{21}) & 0 & \dots & U(r_{2n}) \\ \vdots & \vdots & \vdots & \vdots \\ U(r_{n1}) & U(r_{n2}) & \dots & 0 \end{pmatrix} \quad (6)$$

A priori knowledge of the initial and final points allowed calculating the coefficients a_1, a_2, a_3, a_4 and ω_i in (4) through the relationship:

$$L^{-1}Q = [W \quad a_1 \quad a_2 \quad a_3 \quad a_4]^T \quad (7)$$

where $L = \begin{bmatrix} K & P \\ P^T & O \end{bmatrix}$ with $O = \begin{pmatrix} 0 & 0 & 0 \\ 0 & 0 & 0 \\ 0 & 0 & 0 \end{pmatrix}$, $W = (\omega_1 \ \dots \ \omega_i \ \dots \ \omega_n)$ and $q = \begin{pmatrix} x_1 \\ \vdots \\ x_i \\ \vdots \\ x_n \\ 0 \\ 0 \\ 0 \end{pmatrix}$ represents the coordinates of the control points.

As a result of mesh morphing optimizations through trials and errors, 1110 control points, i.e. 10% of the total mesh points, were randomly sampled on the statistical shape and patient-specific geometrical models, and they were used for the TPS algorithm that transformed the generic FE mesh into the patient-specific FE models. The result was a regularized dense and continuous deformation field that could be applied to any point of the generic FE model, and deform this model towards the patient-specific geometrical 3D model obtained with 3D Shaper. By construction, both models had always the same number of nodes and one to one correspondence. Additional information on the thin plate spline for morphing operations can be found in Bookstein [27] and Singh et al. [29].

2.3.4. Mechanical properties

The vBMD distribution for the 3D structure of the femur obtained in Section 2.3.1 was used to calculate the local stiffness of the bone. A power law was selected for the relationship between bone stiffness and BMD. As such, for the cortical bone, the Young's modulus ($E_{cortical}$), in MPa, was defined by using the following expression [30]:

$$E_{cortical} = 10200\rho_{ash}^{2.01} \quad (8)$$

where ρ_{ash} is the ash density of the bone, in g/cm^3, defined by the relation [21]:

$$\rho_{ash} = 0.87\rho_{QCT} - 0.079 \quad (9)$$

where ρ_{QCT} is the radiological density that was approached using the vBMD values in g/cm^3 obtained in the 3D-Shaper modelling process.

For the trabecular bone, the Young's modulus, in MPa, is given by the equation [31]:

$$E_{trabecular} = 0.003715\rho_{app}^{1.96} \quad (10)$$

where ρ_{app} is the apparent density of the bone, in kg/m^3, that is related to ρ_{ash} according to the expression [21]:

$$\rho_{app} = \frac{\rho_{ash}}{0.6} \quad (11)$$

All femur tissues, i.e. cortical and trabecular bone, were modelled as linear isotropic elastic with Poisson's ratio of 0.3 [32].

2.3.5. Boundary conditions

Lateral fall was simulated for both fracture and control specimens. The fall force was medio-lateral and was distributed on the medial nodes of the femoral head. The distal extremity of the model was fixed, and the surface of the greater trochanter was constrained in the direction of the force (Fig. 3).

The fall force used in the simulations was patient-specific and considered patient mass and weight according to the following expression [33]:

$$F_{fall} = \sqrt{2 \bullet g \bullet h_c \bullet k_{tissue} \bullet m} \quad (12)$$

where g is the gravity acceleration field (9.81 m/s^2), k_{tissue} is a constant related to the unidirectional stiffness of the soft tissues that cover the trochanter (71 N/mm) [34], m is the mass of the patient, and h_c is the height of the centre of gravity related to the height of the patient h, in meters, given by:

$$h_c = 0.51 \bullet h \quad (13)$$

The average values of vBMD, maximum principal strains, major principal strains (MPE), strain energy density (SED), maximum principal stresses and major principal stresses (MPS), per element, were evaluated by fracture zones (trochanteric and neck areas) and tissue (trabecular and cortical bone) (Fig. 4). MPE and MPS represent the highest absolute eigenvalues of the Green-Lagrange strain tensor and of the 2nd Piola-Kirchhoff stress tensor, respectively. All finite element calculations were performed with ABAQUS v2018 (Dassault Systèmes Simulia Corp., Johnston, RI, USA).

2.4. Statistical analysis

A three-ways Multivariate ANOVA was used for the analysis of the neck and trochanteric fractures. Statistical tests and analyses were performed with the software SPSS (IBM). The tests evaluated the

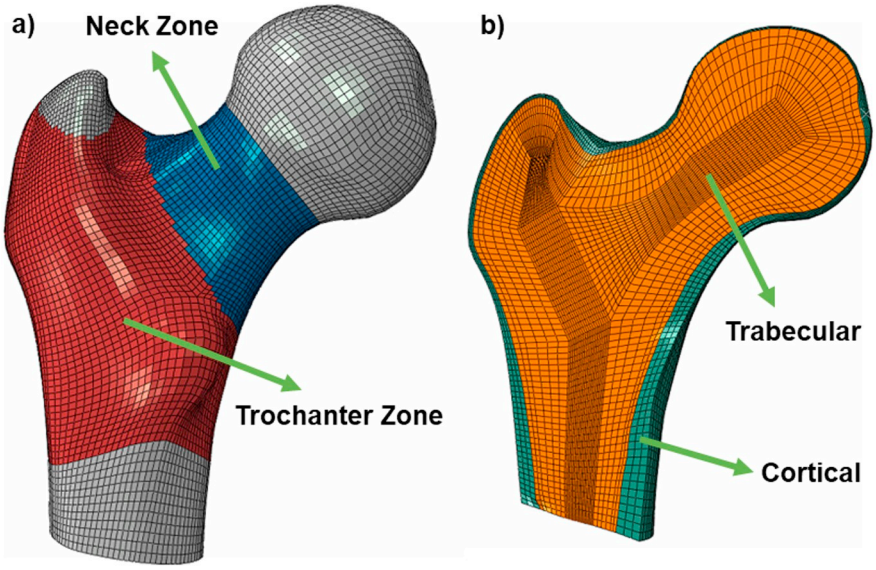

Fig. 4. Analysis zones in the model: a) fracture areas and b) tissues areas.

influence of the factors, for which two levels were defined: (a) *group* (fracture and control), (b) *tissue* (trabecular and cortical), and (c) *gender/sex* (female and male) on the biomechanical descriptor calculated by the FE simulations (dependent variables). In the current study, the dependent variables evaluated were: vBMD obtained by 3D-Shaper as bone intrinsic property, and the maximum principal strain, the major principal strain (MPE), the strain energy density (SED), the maximum principal stress and the major principal stress (MPS), all obtained from the fall FE simulations.

Null hypothesis (H_0) was that no factors have effect over the dependent variables, meaning that *group*, *tissue*, nor *gender/sex* had any effect over the dependent variables. In case of H_0 acceptance for any of the factors, all the measurements would be pooled for the next steps of the analysis. Rejection of H_0 shows a relation between the dependent variable and the factor, implying different behaviours for the two levels of the factor. For this reason, in case of rejection of H_0, the two levels of the factor were considered separately in the following steps of the analysis. The test also evaluated the interactions among factors.

Since more dependent variables were tested, a Bonferroni correction for repetitive tests was used. To keep a familywise (global) error of 5% ($p_{fwe} = 0.05$), each analysis was deemed to be significant at a threshold $p = .008$.

2.5. Discrimination method

The ability of the descriptors statistically analysed in Section 2.4 to discriminate fracture and non-fracture cases was assessed by using the receiver operative characteristic (ROC) curve method. The curve plots the sensitivity, $1 - \beta$ where β is the rate of false negatives, against the rate of false positive, α, and the curve obtained can be compared with the non-discriminating curve, i.e. the bisection of the $(1 - \beta, \alpha)$ space.

Accordingly, the area under the ROC curve (ROC-AUC) measures the discrimination power of the single descriptor selected for the classification. As such, the closer the ROC-AUC value is to 1 the better the discrimination is. On the contrary, values close to 0.5 stand for the area under the non-discriminating curve and indicate a completely random discrimination of the selected descriptor. ROC-AUC values between 0 and 0.5 identify the same discrimination power as their symmetric equivalent between 0.5 and 1, but with inverted classes.

The descriptors evaluated in this section were the vBMD that is DXA-derived, and the descriptors derived from the FE simulations, i.e. the maximum principal strain, major principal strain (MPE), the strain energy density (SED), maximum principal stress and major principal stress (MPS). The features that will be used for the ROC-AUC evaluation will come from the multivariate ANOVA.

The analysis was performed for each descriptor individually and cross-validated by dividing the sample size into n random groups and by repeating the ROC-AUC analysis n times with one of the groups out. The choice of n depended on the numerosity of the sample size. The results of the statistical analysis in Section 2.4 identified the specific of levels and combinations thereof, for which the ROC-AUC analysis results would be most meaningful or clearly interpretable.

3. Results

3.1. Subject recruitment

One hundred and eleven subjects with osteoporosis and older than 50 years, including women and men, were selected. The patients were divided into two groups: the fracture group included 62 patients with a single fracture of the proximal femur (neck or trochanteric fracture), the control group included 49 patients without fracture. The factures were all subsequent to fall, and the group consisted of 36 neck fractures and 26 trochanteric fractures (Table 1).

3.2. FE model generation

The computational times for the generic models evaluated in the convergence study were: 6, 51 and 720 min for Model 1, 2, and 3 respectively on the desktop computer. Even though Model 1 allowed identifying regions of maximum SED that were consistent with the other models (Fig. 5), the SED values in these regions were not converging towards the values achieved with models 2 and 3. Model 2 and Model 3 results were comparable, with relative difference of 5% in SED values and a computational cost significantly lower for Model 2 than for

Table 1
Number of subjects by group and gender/sex.

Group	Total	Women	Men
Fracture	62	45	17
Neck fracture	36	26	10
Trochanter fracture	26	19	7
Control	49	37	12

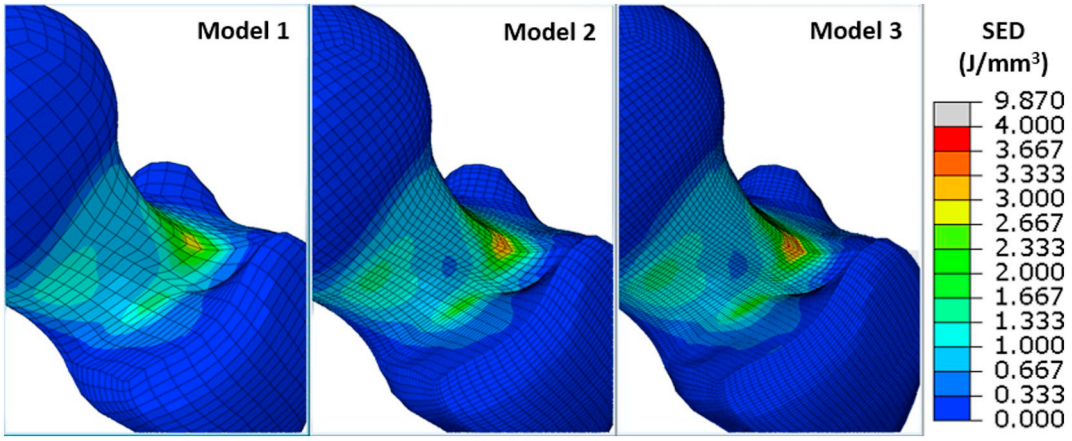

Fig. 5. Strain energy density (SED) results for the convergence test of Models 1, 2 and 3.

Model 3. As such, Model 2 mesh was selected for the study.

The quality of the mesh obtained by the morphing process was controlled to avoid any negative Jacobians due to element distortion during the simulations. In addition, the cortical thickness and volume of the trabecular bone were examined visually in all morphed models. Such examinations confirmed the reproducibility and quality of the geometrical fits of the transformed FE model to the patient-specific geometries obtained by the 3D-Shaper.

The average fall forces obtained for patients with and without fracture were 8666 ± 929 N and 8652 ± 843 N, respectively. No statistical differences were found between the fall forces in fracture and control patients.

3.3. Statistical analysis

3.3.1. Three-way multivariate ANOVA

The vBMD values showed significant differences in both types of fracture for gender/sex and tissue (Tables 2 and 3). The strain and MPE values had differences for tissue and gender/sex. The values for the strain energy density (SED) showed differences for both types of fracture in tissue and gender/sex, and in the interaction tissue-gender/sex for neck fractures cases. The results also revealed that both types of fractures showed differences in the values obtained for the stress and MPS in group, tissue, gender/sex, interaction tissue-gender/sex. The stress values also showed significant differences in the interaction group-tissue. Finally, the overall multivariate analysis showed significant differences in all values for group, tissue and gender/sex variations, and in the interactions between group and tissue and between tissue and gender/sex for both neck and trochanteric fractures (Tables 2 and 3).

3.3.2. Descriptive statistics

Comparing the different groups, the mean vBMD in the cortical bone was lower than 1 g/cm^3 independently of the group, location of the fracture and gender/sex (Tables 4, 5). All the descriptor values computed for neck fractures were lower than the values calculated for the control cases. Similar results were obtained with the trochanter fracture cases. Major differences between fractures and controls were obtained with the MPS values, for both types of fractures (Tables 4, 5). The differences in the descriptors values between groups were higher for trochanter than for neck fractures.

As for the differences between tissues, the MPS values in the trabecular bone were higher than 10 MPa in 77% of the control cases and 40% of the fracture cases. As for the cortical bone, 37% of the control cases and 55% of the fracture cases presented values higher than 100 MPa.

3.4. ROC-AUC analyses

Based on the results obtained in the statistical analysis, the ROC-AUC method was applied considering the type of bone, gender/sex, and type of fracture. The identified statistically significant difference in gender/sex requires to run a different analysis for male and female. However, the number of men in the database for each fracture was very small compared with women (Table 1) and the ROC-AUC method was not applied in men to avoid misinterpretations of the results. Since a different sample size was achieved for the two groups of neck and trochanteric fractures, the cross-validation was applied using different numbers of group: 5 groups for subjects with neck-fracture and 4 groups for subjects with trochanter fracture. The results of the ANOVA analysis also required to run separate ROC-AUC analyses for the two different types of bone tissue: trabecular and cortical.

Table 2
3-ways ANOVA results by descriptor for neck fracture cases. Values lower than the significance threshold (.008) are highlighted in bold.

Feature	vBMD (g/cm^3)		Maximum principal strain (mm/mm)		Major principal strain (MPE) (mm/mm)		Strain energy density (SED) (J/mm^3)		Maximum principal stress (MPa)		Major principal stress (MPS) (MPa)		Multivariate		
	p-Value	Power	p-Value	Power	p-Value	Power	p-Value	Power	p-Value	Power	p-Value	Power	p-Value	Power	Fisher coefficient
Group	**.0046**	0.8166	.0205	0.6436	.0397	0.5407	.0136	0.6997	**.0008**	0.9267	**.0036**	0.8366	**.0000**	0.9967	5.692
Tissue	**.0000**	1.0000	.3255	0.1652	**.0000**	0.9996	**.0000**	1.0000	**.0000**	1.0000	**.0000**	1.0000	**.0000**	1.0000	2280.495
Gender/sex	.2730	0.1941	**.0000**	0.9930	**.0000**	0.9961	**.0000**	0.9955	**.0001**	0.9834	**.0000**	0.9982	**.0000**	0.9987	6.345
Group * tissue	.4043	0.1320	.5400	0.0936	.8488	0.0541	.0498	0.5021	**.0020**	0.8803	.0242	0.6190	**.0005**	0.9798	4.374
Group * gender/sex	.7421	0.0624	.3523	0.1527	.4534	0.1159	.1236	0.3370	.2877	0.1853	.1596	0.2895	.4773	0.3568	0.928
Tissue * gender/sex	.8446	0.0544	.4047	0.1319	.4466	0.1180	**.0001**	0.9773	.0002	0.9665	**.0000**	0.9886	**.0000**	0.9977	5.944
Group * tissue * gender/sex	.6621	0.0719	.6099	0.0800	.6768	0.0699	.1664	0.2819	.3467	0.1552	.2168	0.2340	.6797	0.2563	0.663

Table 3
3-ways ANOVA results by descriptor for trochanteric fracture cases. Values lower than the significance threshold (.008) are highlighted in bold.

Feature	vBMD (g/cm^3)		Maximum principal strain (mm/mm)		Major principal strain (MPE) (mm/mm)		Strain energy density (SED) (J/mm^3)		Maximum principal stress (MPa)		Maximum principal strain (mm/mm)		Multivariate		
	p-Value	Power	p-Value	Power	p-Value	Power	p-Value	Power	p-Value	Power	p-Value	Power	p-Value	Power	Fisher coefficient
Group	**.0008**	0.9311	.5955	0.0824	.4791	0.1083	.2731	0.1936	.0091	0.7504	.1299	0.3275	**.0000**	0.9992	6.831
Tissue	**.0000**	1.0000	**.0000**	1.0000	**.0000**	1.0000	**.0000**	1.0000	**.0000**	1.0000	**.0000**	1.0000	**.0000**	1.0000	1934.052
Gender/sex	.4800	0.1081	**.0007**	0.9352	**.0008**	0.9299	**.0002**	0.9716	**.0001**	0.9860	**.0002**	0.9691	**.0002**	0.9894	4.963
Group ∗ tissue	.7012	0.0668	.9746	0.0501	.5686	0.0875	.7221	0.0644	.0213	0.6399	.5603	0.0891	**.0002**	0.9883	4.891
Group ∗ gender/sex	.4068	0.1308	.4259	0.1243	.5071	0.1011	.6428	0.0746	.6903	0.0681	.9269	0.0510	.8976	0.1498	0.368
Tissue ∗ gender/sex	.6685	0.0710	.2334	0.2206	.0857	0.4050	.0253	0.6142	**.0003**	0.9611	**.0020**	0.8808	**.0015**	0.9608	3.929
Group ∗ tissue ∗ gender/sex	.5783	0.0856	.4791	0.1083	.5084	0.1008	.9089	0.0515	.7076	0.0660	.9415	0.0506	.9748	0.1005	0.204

The MPS was the biomechanical descriptor with highest ROC-AUC values for both neck and trochanteric fractures. Indeed, in the trabecular bone AUC values were 0.81 and 0.91 for neck and trochanteric fractures, respectively (Fig. 6). For trochanteric fractures and trabecular bone, the stress and SED led to ROC-AUC values higher than 0.80 (Table 6). Strain-related descriptors associated with the lowest ROC-AUC values in the trabecular bone and in the cortical bone (trochanteric fracture). In the cortical bone and for neck fracture cases, the vBMD was the least discriminating descriptor. In general, 5 out of the 6 studied descriptors led to ROC-AUC values higher than 0.70 for the discrimination of neck fracture (Table 6). In the trochanteric fracture group, the ROC-AUC values were generally higher for the descriptors calculated in the trabecular bone than for those calculated in the cortical bone, except for the vBMD. In the neck fracture group, the vBMD, stress and MPS led to higher ROC-AUC values in the trabecular than in the cortical bone.

4. Discussion

The fall loads used in the simulations were patient-specific. Applying a load that simulated the condition of fracture due to lateral fall in fracture and control cases allowed us finding the best descriptors that describe the behaviour of the bone in such condition. As such, we could further evaluate these descriptors for fracture discrimination.

The bone as an organ has anisotropic and inhomogeneous material properties. The consideration of such anisotropy by using micromechanic-derived properties from CT data has been implemented in FE model of a mandible [35,36]. On one hand, the results of such analyses revealed the importance of considering bone anisotropy in FE simulations for strain and displacements estimations. On the other hand, the study of Baca et al. [37] suggested that organ-level analyses of the proximal femur, as the one performed in our study, isotropic material properties can be used instead of orthotropic inhomogeneous material model. Also, the study of Yosibash et al. [38] showed slight differences for the estimated strain and displacement obtained by simulation using: a) isotropic and b) orthotropic inhomogeneous formulation for the material properties of bone for stance simulations. Accordingly, Taghizadeh et al. [39] estimated that not considering anisotropy would lead to errors of about 7% in terms of displacement and ultimate force predictions. Arguably, this error might be larger in terms of local stress/strain fields and local errors might also depend on specific combinations of organ geometries and boundary loads. It is worth to mention that the values evaluated with the ROC-AUC are not absolute but relative between two populations, i.e. fracture and non-fracture cases, simulated in the same way.

The bone elastic properties defined in our study came from empirical relationships [21,30,31] where the Young modulus was defined as the slope of the linear part of the bone loading stress-strain curve under axial compression [30]. Arguably load-rate independent Young's moduli, consistent with ultrasound measurements [40], are rather obtained in the unloading compressive regime [41]. Hence, our elasticity values might rather reflect elastoplastic hardening moduli, the physics of which is unlikely to be captured by empirical Eq. (8) [30]. Such considerations become important when simulations are used to understand the bone mechanical behaviour and failure mechanisms. However, this is beyond the scope of the present study, where we pragmatically assume a purely elastic bone material in which the loading and unloading curve stress-strain should coincide. Accordingly, we tackle the specific modelling of osteoporotic bone. In such a case, fragile fractures do not present post-elastic behaviour and constitutive material equations can be limited to the elastic range [42]. Another point to consider is the large strain values obtained from our

Table 4
Neck fracture descriptive statistics.

Descriptor	Tissue	Control				Fracture			
		Female (N = 26)		Male (N = 10)		Female (N = 26)		Male (N = 10)	
		Mean	Std. deviation	Mean	Std. deviation	Mean	Std. deviation	Mean	Std. deviation
vBMD (g/cm^3)	Trabecular	0.149	0.044	0.150	0.037	0.120	0.025	0.131	0.027
	Cortical	0.763	0.034	0.772	0.026	0.751	0.035	0.759	0.034
Maximum principal strain (mm/mm)	Trabecular	0.022	0.008	0.017	0.006	0.019	0.008	0.015	0.005
	Cortical	0.023	0.006	0.014	0.005	0.017	0.007	0.012	0.004
Major principal strain (MPE) (mm/mm)	Trabecular	0.0499	0.0206	0.0354	0.0106	0.0433	0.0173	0.0305	0.0111
	Cortical	0.0350	0.0082	0.0222	0.0078	0.0273	0.0094	0.0204	0.0077
Strain energy density (SED) (J/mm^3)	Trabecular	0.412	0.189	0.246	0.077	0.267	0.161	0.169	0.063
	Cortical	4.45	1.81	1.99	1.11	2.87	1.72	1.66	1.08
Maximum principal stress (MPa)	Trabecular	3.99	1.11	2.71	0.68	2.78	1.11	2.24	0.52
	Cortical	86.94	22.72	56.70	18.18	60.78	27.55	42.77	12.28
Major principal stress (MPS) (MPa)	Trabecular	17.27	3.82	12.38	2.71	12.11	4.43	9.31	1.33
	Cortical	198.84	41.32	127.59	44.44	151.27	52.23	112.01	38.09

Table 5
Trochanteric fracture descriptive statistics.

Descriptor	Tissue	Control				Fracture			
		Female (N = 19)		Male (N = 7)		Female (N = 19)		Male (N = 7)	
		Mean	Std. deviation	Mean	Std. deviation	Mean	Std. deviation	Mean	Std. deviation
vBMD (g/cm^3)	Trabecular	0.115	0.036	0.128	0.017	0.096	0.027	0.087	0.022
	Cortical	0.767	0.042	0.779	0.030	0.745	0.044	0.752	0.036
Maximum principal strain (mm/mm)	Trabecular	0.030	0.010	0.020	0.005	0.026	0.011	0.021	0.010
	Cortical	0.012	0.003	0.009	0.002	0.011	0.004	0.008	0.002
Major principal strain (MPE) (mm/mm)	Trabecular	0.061	0.019	0.039	0.009	0.052	0.023	0.040	0.019
	Cortical	0.018	0.005	0.012	0.002	0.017	0.007	0.012	0.003
Strain energy density (SED) (J/mm^3)	Trabecular	0.514	0.186	0.269	0.080	0.288	0.160	0.172	0.110
	Cortical	1.36	0.61	0.635	0.199	1.24	0.93	0.591	0.284
Maximum principal stress (MPa)	Trabecular	3.19	0.44	2.40	0.35	2.60	0.77	1.89	0.64
	Cortical	49.83	12.04	34.84	7.79	39.92	11.35	27.59	8.86
Major principal stress (MPS) (MPa)	Trabecular	12.75	1.81	9.90	1.17	8.91	2.44	6.20	2.18
	Cortical	97.68	22.63	68.88	10.05	88.57	33.22	61.09	16.00

Table 6
ROC-AUC values (average from cross-validation) for women by zone of fracture and type of tissue.

Descriptor	Neck		Trochanter	
	Trabecular	Cortical	Trabecular	Cortical
vBMD	0.70	0.59	0.61	0.64
Maximum principal strain	0.60	0.71	0.64	0.59
Major principal strain (MPE)	0.58	0.73	0.66	0.58
Strain energy density (SED)	0.72	0.74	0.84	0.62
Maximum principal stress	0.77	0.75	0.83	0.73
Major principal stress (MPS)	0.81	0.74	0.91	0.67

simulations. While such values might fall out of the elastic range of the mechanical behaviour of bone, our bone material model ignored any elastoplastic/damage effects on the effective tissue stiffness. As mentioned earlier, we did not aim to simulate fracture events, but this limitation might partly explain why our strain-based descriptors performed so poorly in terms of fracture and non-fracture cases discrimination.

The apparent BMD for the trabecular bone in our study was obtained using the Eq. (11) [21]. Hernandez et al. [43] reported a ratio of 0.60 for ash/app density for low density trabecular tissue. All the subjects in our study have osteoporosis and the average values of trabecular bone density reflect relatively low-density tissues, i.e. from 0.125 ± 0.025 g/cm^3 to 0.131 ± 0.027 g/cm^3. As such, the trabecular density in our study can be considered as low-density distribution where the relation ash/app of 0.6 of Eq. (11) can be applied. Regarding the ash density, Gong et al. [44] reported a loss of 6.6% of hydroxyapatite during the ashing procedures. The ROC_AUC calculations were repeated using a corrected ash density, i.e. $\rho_{ash,\ c} = 1.066\rho_{ash}$, to consider the loss of hydrocyapatite. The discrimination ROC-AUC values obtained with the corrected ash density were exactly the same as the one obtained without correction (data not shown). As such, the 6.6% of hydroxyapatite that might be lost by incineration, would not affect the discrimination outcomes of our study.

Many hip fracture studies focus only on women [9,14,15,22,45,46]. Our statistical analysis revealed significant differences between women and men in terms of descriptor values obtained through FE simulations. In this sense, Keyak et al. [47] highlighted the consideration of sex differences when FE analyses are performed in the study of hip fracture. They found that the difference between the strengths obtained by FE simulations for fracture and control patients was greater in men than in women. Dall'Ara et al. [48] used a population data that considered women and men together to validate a femur FE model. Nevertheless, the analysis of the effect of the gender/sex was out of the scope of their results. Our ANOVA results indicate that males and females should be analysed separately. Unfortunately, the number of males in our cohort was relatively small and to avoid misguided interpretation of the results, the ROC-AUC outcomes were only analysed for the female population. A large population of men would provide a better understanding of the relevance of gender/sex differences in FE-based fracture classification.

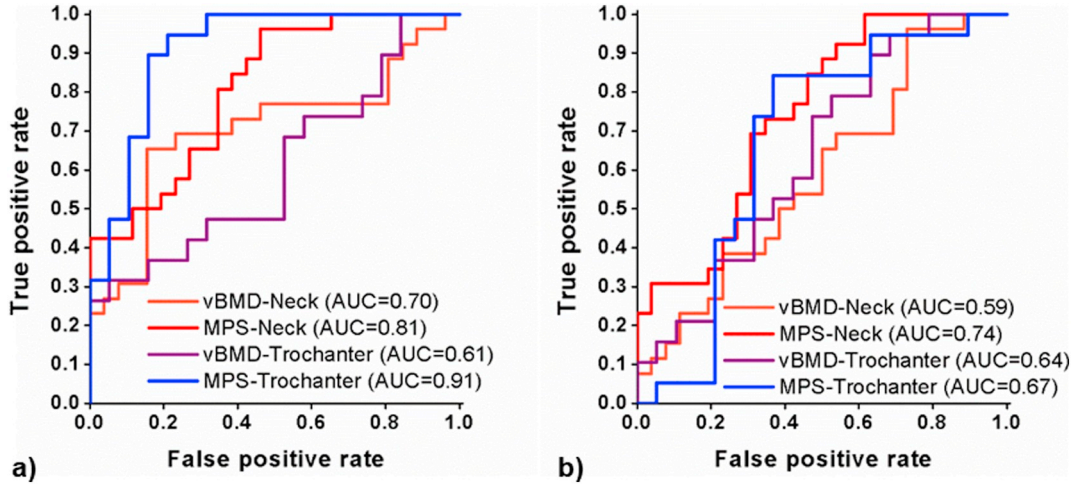

Fig. 6. ROC curve for volumetric BMD (vBMD) and major principal stress (MPS) by type of fracture at: a) the trabecular bone and b) the cortical bone.

The ANOVA results showed significant differences in the values for tissue, i.e. trabecular and cortical bone, in all descriptors evaluated. Nowadays there is no consensus about whether the fracture initiates in the trabecular or in the cortical bone. The gradual and non-homogeneous degeneration of both tissues during ageing generates a situation of global fragility. Due to its porous structure, the trabecular bone has lower stiffness and yield stress than the cortical bone but it withstands higher deformations than the latter, at the millimetric scale. Overall, the two tissues form a synergic mechanical system and it is difficult to systematically relate the occurrence of fracture to any specific single tissue. Yet, our study shows that the significant interaction between the kind of tissue and the fracture group, meaning that each tissue changes its mechanical behaviour depending on the group of analysis (fracture or not). In particular, the cortical bone bears high stresses in more cases of the fracture group than of the control group, whereas, for the trabecular bone the result is the opposite. This result suggests that the cortical bone mechanically shield the weakened trabecular bone structure. Because of the phenomenological and non-unique character of the relationships used to relate together bone density and stiffness [49], it is difficult to quantitatively assess any risk of bone fracture based on any cortical or trabecular bone strength value. Nevertheless, our ROC-AUC analyses strongly supports the idea that trabecular bone mechanical weakening is a better descriptor for fracture risk discrimination than cortical bone overload (AUC 0.81 in neck 0.91 in trochanter). It is worth to mention that the path for the load transmission between cortical and trabecular bone, and the location of the beginning of the fracture were out of the scope of our study.

The areal BMD measured through DXA is the gold standard for diagnosis of osteoporosis [13]. Also, this descriptor was used for discrimination of fracture cases with a ROC-AUC value of 0.66 [14], which reflects a relatively poor discrimination power. As a result, the possible use of DXA areal BMD as a discriminator for fracture and non-fracture cases or fracture predictor is questionable. Moreover, our results showed that using the vBMD obtained by 3D Shaper did not really improve this power of discrimination (ROC-AUC value of 0.70 in the best case) in comparison with other descriptors, e.g. MPS. Indeed, for the combinations neck fracture and cortical bone, and trochanter fracture and trabecular bone, vBMD led to our lowest calculated ROC-AUC values. Previous studies already reported that QCT-based FE-estimated femur strength is a better descriptor than the areal BMD for fracture risk assessments [4,16,20]. Our results are aligned with this statement.

DXA-based FE femur models developed in the last years focused on the study of hip fractures [3,9,14,25,45,48]. For fracture discrimination, Yang et al. [9] created DXA-based 2D FE femur models which provided a ROC-AUC value of 0.82 for trochanteric fractures using the FE-derived descriptor called index of fracture risk as a discriminator. Naylor et al. [14], used the FE-derived femoral strength obtained with 2D DXA-based models to discriminate fractures cases. They found a ROC-AUC value of 0.68 which can be considered as poor-fair value for discrimination. Recently, Grassi et al. [25] highlighted the advantages of building a 3D model from DXA images, even though model estimation accuracy of the bone strength was lower than QCT-based 3D models. Our ROC-AUC result for the MPS generally showed higher values (0.81 and 0.91) for neck and trochanter fractures than the ones obtained with 2D DXA-based models. This result sand for a first proof-of-concept that 3D-DXA models can predict valuable biomechanical descriptors that integrate the respective effects of 3D shapes, tissue volumetric heterogeneity and quality, and boundary loads, to eventually improve the capacity of fracture case discrimination.

As for the descriptors used for fracture discrimination, several numerical studies used femoral strength or load-to-strength ratio as descriptors for fracture discrimination [14,15,50]. The femoral strength was defined as the load needed to overcome a hypothetical critical strain that leads to organ failure [15]. Considering the critical strain as constant for the entire bone might not capture the mechanical environment involved in fracture initiation and catastrophic propagation, since critical strains for cortical and trabecular bone are different. Also, mechanical failure parameters for the trabecular bone are very heterogeneous since they locally change with tissue density [51] or structure [52]. Our study shows, for the first time, that the relatively good fracture discrimination can be obtained by using the MPS descriptor as a discriminator, without any a priori knowledge of specific threshold values.

The best outcomes in terms of fracture classification have been usually achieved with QCT-based 3D proximal femur FE models. Orwoll et al. [50] and Qasim et al. [15] used 3D QCT-based models obtaining maximum ROC-AUC values of 0.83 and 0.79 respectively. Nishiyama et al. [22] addressed the classification of fracture and non-fracture cases by type of fracture using QCT-based 3D femur FE models. They reported ROC-AUC values of 0.79 and 0.94 for trochanter and neck fracture respectively, using the failure load as a classifier. Our discrimination results using DXA-based 3D FE models, led to higher ROC-AUC value for trochanteric fracture, 0.91, and a lower value for neck fracture, 0.81. The MPS is evaluated in the trabecular bone in both cases. Nevertheless, the ROC-AUC analyses of Nishiyama et al. [22] might be more data dependent and less robust, therefore, than ours, since the number of female patients with fracture was 35, which was 22% lower than the one used in our study (45 women with fracture). Another point to consider is that Nishiyama et al. [22] did not separate the bone into cortical and trabecular, which might additionally affect the robustness of their results, according to the outcomes of our statistical analyses. In addition, we applied a 5-folds and a 4-folds cross validation for the neck and trochanter fracture discriminations, respectively. Our ROC-AUC results remained very similar, which confirmed the relatively good homogeneity of the data used and suggests that our study is robust for the study of fracture. Overall, our ROC-AUC values, obtained through DXA-based 3D FE models are comparable to the ones obtained by using QCT-based FE models, which stands for a clear progress towards safe personalised assessments of the risk of fracture during patient screening and follow-ups.

Despite the positive outcome in terms of fracture discrimination, the present study has some limitations. First, the composition of the bone was not robustly included in the model since our relationship between density and stiffness are empirical and may suffer great variations [49]. Modelling studies at the micrometric scale showed that the matrix of stiffness of the bone can be obtained from forward calculations based on the composition of the bone, e.g. water, organic and mineral content [35,53]. This achievement might be extrapolated [54] to the tissue level, i.e. the millimetric scale, to obtain the 3D distribution of bone stiffness within the femur. Secondly, the angle of force application remained constant, while variations of the application force angle might have influenced the strain and displacement outcomes obtained by the FE model as reported in a previous study [55]. Such aspect needs to be explored in a next study. Third, more patients should be included in the study to increase the power of the analysis. The increment of patient number would provide a better understanding and extrapolation of the results obtained. Finally, all models were patient-specific, but no geometrical parameter nor age were explicitly included as independent descriptors for the discrimination. Both the factor and the control groups were age-matching, and the ranges of patient age were relatively narrow. Hence, the use of the age as a variable was not appropriated. Though MPS calculations actually integrate geometrical effects, Testi et al. [45] reported that fracture classification improves by combining geometrical parameters and FE results. In this sense, a more sophisticated method for classification, e.g. support vector machines, should be explored. However, in patient-specific FE modelling, as performed in this study, geometry and age effects are always indirectly part of the analyses, since local MPS calculations largely depend on geometry effects and on the tissue material properties. On one hand, the model geometries are patient-specific. On the other hand, the material properties depend on the BMD, the distributions and magnitudes of which

are also patient-specific in the models and depend on both age and tissue condition.

5. Conclusions

This study showed that DXA-based 3D FE models of proximal femur can be used for the discrimination of hip fracture cases versus no-fracture controls. Biomechanical descriptors obtained through FE simulations integrate femur shape, cortical thickness, and volumetric distribution of BMD from 3D Shaper and improved the discrimination of facture occurrence compared to the classical use of areal BMD or compared to vBMD. As a result, the fracture discrimination achieved in the present study was not based exclusively on densitometry data. Analyses by type of bone, type of fracture and gender/sex are the key to obtain high accuracy in the discrimination of patient with fracture from the ones without fracture. The fact that DXA is less invasive than QTC makes possible the use of DXA-based 3D FE model in clinical practice as a routine patient screening. The power of DXA-based 3D modelling and FE simulations in terms of fracture risk prediction should be further explored.

Acknowledgements

Financial funding from the Spanish Government's MINETUR (DENSI3D-TSI-100101-2013-109) and MINECO (BioDXA-RTC-2014-2740-1, RYC-2015-18888) are acknowledged.

References

[1] K. Imai, Recent methods for assessing osteoporosis and fracture risk, Recent Pat. Endocr., Metab. Immune Drug Discovery 8 (1) (2014) 48–59.
[2] World Health Organization, Assessment of fracture risk and its application to screening for postmenopausal osteoporosis. Report of a WHO Study Group, World Health Organ. Tech. Rep. Ser. 843 (1994) 1–129.
[3] Y. Luo, Z. Ferdous, W.D. Leslie, A preliminary dual-energy X-ray absorptiometry-based finite element model for assessing osteoporotic hip fracture risk, Proc. Inst. Mech. Eng. H J. Eng. Med. 225 (12) (2011) 1188–1195.
[4] J.H. Keyak, et al., Effect of finite element model loading condition on fracture risk assessment in men and women: the AGES-Reykjavik study, Bone 57 (1) (2013) 18–29.
[5] P. Kannus, J. Parkkari, H. Sievänen, A. Heinonen, I. Vuori, M. Järvinen, Epidemiology of hip fractures, Bone 18 (1 Suppl) (Jan. 1996) 57S–63S.
[6] O. Johnell, J.A. Kanis, An estimate of the worldwide prevalence and disability associated with osteoporotic fractures, Osteoporos. Int. 17 (12) (2006) 1726–1733.
[7] R. Burge, B. Dawson-Hughes, D.H. Solomon, J.B. Wong, A. King, A. Tosteson, Incidence and economic burden of osteoporosis-related fractures in the United States, 2005–2025, J. Bone Miner. Res. 22 (3) (2007) 465–475.
[8] International Osteoposis Foundation, Osteoporosis - incidence and burden, [Online]. Available: https://www.iofbonehealth.org.
[9] L. Yang, N. Peel, J.A. Clowes, E.V. McCloskey, R. Eastell, Use of DXA-based structural engineering models of the proximal femur to discriminate hip fracture, J. Bone Miner. Res. 24 (1) (2009) 33–42.
[10] F. Cosman, et al., Clinician's guide to prevention and treatment of osteoporosis, Osteoporos. Int. 25 (10) (2014) 2359–2381.
[11] S. Drew, A. Judge, C. Cooper, M.K. Javaid, A. Farmer, R. Gooberman-Hill, Secondary prevention of fractures after hip fracture: a qualitative study of effective service delivery, Osteoporos. Int. 27 (5) (2016) 1719–1727.
[12] A.H.K. Riemen, J.D. Hutchison, The multidisciplinary management of hip fractures in older patients, Orthop. Trauma 30 (2) (2016) 117–122.
[13] Z. Li, A.A. Chines, M.P. Meredith, Statistical validation of surrogate endpoints: is bone density a valid surrogate for fracture? J. Musculoskelet. Neuronal Interact. 4 (1) (2004) 64–74.
[14] K.E. Naylor, E.V. McCloskey, R. Eastell, L. Yang, Use of DXA-based finite element analysis of the proximal femur in a longitudinal study of hip fracture, J. Bone Miner. Res. 28 (5) (2013).
[15] M. Qasim, et al., Patient-specific finite element estimated femur strength as a predictor of the risk of hip fracture: the effect of methodological determinants, Osteoporos. Int. (June) (2016).
[16] P. Zysset, et al., Clinical use of quantitative computed tomography-based finite element analysis of the hip and spine in the management of osteoporosis in adults: the 2015 ISCD official positions-part II, J. Clin. Densitom. 18 (3) (2015) 359–392.
[17] O.M. Babatunde, A.T. Fragomen, S.R. Rozbruch, Noninvasive quantitative assessment of bone healing after distraction osteogenesis, HSS J. 6 (1) (2010) 71–78.
[18] M.G. Donaldson, L. Palermo, J.T. Schousboe, K.E. Ensrud, M.C. Hochberg, S.R. Cummings, FRAX and risk of vertebral fractures: the fracture intervention trial, J. Bone Miner. Res. 24 (11) (2009) 1793–1799.
[19] R.P. Heaney, Is the paradigm shifting? Bone 33 (4) (Oct. 2003) 457–465.
[20] P.K. Zysset, E. Dall'ara, P. Varga, D.H. Pahr, Finite element analysis for prediction of bone strength, Bonekey Rep. 2 (August) (2013) 386.
[21] E. Schileo, et al., An accurate estimation of bone density improves the accuracy of subject-specific finite element models, J. Biomech. 41 (11) (2008) 2483–2491.
[22] K.K. Nishiyama, M. Ito, A. Harada, S.K. Boyd, Classification of women with and without hip fracture based on quantitative computed tomography and finite element analysis, Osteoporos. Int. 25 (2) (2014) 619–626.
[23] L. Humbert, et al., 3D-DXA: assessing the femoral shape, the trabecular macrostructure and the cortex in 3D from DXA images, IEEE Trans. Med. Imaging 36 (1) (Jan. 2017) 27–39.
[24] S.P. Väänänen, L. Grassi, G. Flivik, J.S. Jurvelin, H. Isaksson, Generation of 3D shape, density, cortical thickness and finite element mesh of proximal femur from a DXA image, Med. Image Anal. 24 (1) (2015) 125–134.
[25] L. Grassi, S.P. Väänänen, M. Ristinmaa, J.S. Jurvelin, H. Isaksson, Prediction of femoral strength using 3D finite element models reconstructed from DXA images: validation against experiments, Biomech. Model. Mechanobiol. (2016) 1–12.
[26] L. Humbert, J. Hazrati Marangalou, L.M. del Río Barquero, G.H. van Lenthe, B. van Rietbergen, Technical note: cortical thickness and density estimation from clinical CT using a prior thickness-density relationship, Med. Phys. 43 (4) (Mar. 2016) 1945–1954.
[27] F.L. Bookstein, Principal warps: thin-plate splines and the decomposition of deformations, IEEE Trans. Pattern Anal. Mach. Intell. 11 (6) (1989) 567–585.
[28] M.H. Davis, A. Khotanzad, D.P. Flamig, S.E. Harms, A physics-based coordinate transformation for 3-D image matching, IEEE Trans. Med. Imaging 16 (3) (1997) 317–328.
[29] H. Singh, A. Kumar, G. Singh, Image morphing: a literature study, Int. J. Comput. Appl. Technol. Res. 3 (11) (2014) 701–705.
[30] T.S. Keller, Predicting the compressive mechanical behavior of bone, J. Biomech. 27 (9) (1994) 1159–1168.
[31] R. Hodgskinson, J.D. Currey, Young's modulus, density and material properties in cancellous bone over a large density range, J. Mater. Sci. Mater. Med. 3 (5) (1992) 377–381.
[32] E. Schileo, L. Balistreri, L. Grassi, L. Cristofolini, F. Taddei, To what extent can linear finite element models of human femora predict failure under stance and fall loading configurations? J. Biomech. 47 (14) (2014) 3531–3538.
[33] M.L. Bouxsein, P. Szulc, F. Munoz, E. Thrall, E. Sornay-Rendu, P.D. Delmas, Contribution of trochanteric soft tissues to fall force estimates, the factor of risk, and prediction of hip fracture risk, J. Bone Miner. Res. 22 (6) (2007) 825–831.
[34] S.N. Robinovitch, W.C. Hayes, T. a McMahon, Prediction of femoral impact forces in falls on the hip, J. Biomech. Eng. 113 (November 1991) (1991) 366–374.
[35] C. Hellmich, C. Kober, B. Erdmann, Micromechanics-based conversion of CT data into anisotropic elasticity tensors, applied to FE simulations of a mandible, Ann. Biomed. Eng. 36 (1) (2008) 108–122.
[36] C. Kober, B. Erdmann, C. Hellmich, R. Sader, H.F. Zeilhofer, Consideration of anisotropic elasticity minimizes volumetric rather than shear deformation in human mandible, Comput. Methods Biomech. Biomed. Engin. 9 (2) (2006) 91–101.
[37] V. Baca, Z. Horak, P. Mikulenka, V. Dzupa, Comparison of an inhomogeneous orthotropic and isotropic material models used for FE analyses, Med. Eng. Phys. 30 (7) (2008) 924–930.
[38] Z. Yosibash, N. Trabelsi, C. Hellmich, Subject-specific p-FE analysis of the proximal femur utilizing micromechanics-based material properties, Int. J. Multiscale Comput. Eng. 6 (5) (2008) 483–498.
[39] E. Taghizadeh, M. Reyes, P. Zysset, A. Latypova, A. Terrier, P. Büchler, Biomechanical role of bone anisotropy estimated on clinical CT scans by image registration, Ann. Biomed. Eng. 44 (8) (2016) 2505–2517.
[40] C. Morin, C. Hellmich, A multiscale poromicromechanical approach to wave propagation and attenuation in bone, Ultrasonics 54 (5) (2014) 1251–1269.
[41] K.W. Luczynski, A. Steiger-Thirsfeld, J. Bernardi, J. Eberhardsteiner, C. Hellmich, Extracellular bone matrix exhibits hardening elastoplasticity and more than double cortical strength: evidence from homogeneous compression of non-tapered single micron-sized pillars welded to a rigid substrate, J. Mech. Behav. Biomed. Mater. 52 (2015) 51–62.
[42] M. Viceconti, Multiscale Modeling of the Skeletal System, Cambridge University Press, Cambridge, 2011.
[43] C.J. Hernandez, G.S. Beaupré, T.S. Keller, D.R. Carter, The influence of bone volume fraction and ash fraction on bone strength and modulus, Bone 29 (1) (Jul. 2001) 74–78.
[44] J.K. Gong, J.S. Arnold, S.H. Cohn, The density of organic and volatile and non-volatile inorganic components of bone, Anat. Rec. 149 (3) (1964) 319–324.
[45] D. Testi, M. Viceconti, A. Cappello, S. Gnudi, Prediction of hip fracture can be significantly improved by a single biomedical indicator, Ann. Biomed. Eng. 30 (6) (2002) 801–807.
[46] D.D. Cody, F.J. Hou, G.W. Divine, D.P. Fyhrie, Femoral structure and stiffness in patients with femoral neck fracture, J. Orthop. Res. 18 (3) (May 2000) 443–448.
[47] J.H. Keyak, et al., Male-female differences in the association between incident hip fracture and proximal femoral strength: a finite element analysis study, Bone 48 (6) (2011) 1239–1245.
[48] E. Dall'Ara, R. Eastell, M. Viceconti, D. Pahr, L. Yang, Experimental validation of DXA-based finite element models for prediction of femoral strength, J. Mech. Behav. Biomed. Mater. 63 (Oct. 2016) 17–25.
[49] B. Helgason, E. Perilli, E. Schileo, F. Taddei, S. Brynjólfsson, M. Viceconti, Mathematical relationships between bone density and mechanical properties: a literature review, Clin. Biomech. 23 (2) (2008) 135–146.
[50] E.S. Orwoll, et al., Finite element analysis of the proximal femur and hip fracture risk in older men, J. Bone Miner. Res. 24 (3) (2009) 475–483.
[51] J.C. Lotz, T.N. Gerhart, W.C. Hayes, Mechanical properties of trabecular bone from

the proximal femur: a quantitative CT study, J. Comput. Assist. Tomogr. 14 (1) (1990) 111.
[52] J. Wang, et al., Trabecular plate loss and deteriorating elastic modulus of femoral trabecular bone in intertrochanteric hip fractures, Bone Res. 1 (4) (2013) 346–354.
[53] R. Blanchard, A. Dejaco, E. Bongaers, C. Hellmich, Intravoxel bone micromechanics for microCT-based finite element simulations, J. Biomech. 46 (15) (2013) 2710–2721.
[54] R. Blanchard, C. Morin, A. Malandrino, A. Vella, Z. Sant, C. Hellmich, Patient-specific fracture risk assessment of vertebrae: a multiscale approach coupling X-ray physics and continuum micromechanics, Int. J. Numer. Methods Biomed. Eng. 32 (9) (Sep. 2016) e02760.
[55] L. Grassi, et al., Accuracy of finite element predictions in sideways load configurations for the proximal human femur, J. Biomech. 45 (2) (2012) 394–399.